Asian Journal of Chemistry; Vol. 38, No. 8 (2026), 2076-2088
ASIAN JOURNAL OF CHEMISTRY
https://doi.org/10.14233/ajchem.2026.35757

Refinement Rietveld Study of Magnesium-Doped Cobalt Ferrites ($Mg_xCo_{1-x}Fe_2O_4$)/Polyol on Dye Adsorptive Removal

KARISHMA V. SHIKHARE[1], AMOL B. PANDHARE[1], KRANTI K. PATIL[2], RAJENDRA P. PATIL[1,*], WALAA ALHARBI[3], KHADIJAH H. ALHARBI[3], ABDALLAH A. ALOTIBI[4,*] and SAMI M. ABDEL AZEEM[4,5]

[1]Department of Chemistry, M.H. Shinde Mahavidyalaya, Tisangi, Kolhapur-416206, India
[2]Department of Chemistry, Rajaram College, Kolhapur-416408, India
[3]Department of Chemistry, Science and Arts College, King Abdulaziz University, Rabigh, Saudi Arabia
[4]Department of Chemistry, College of Science and Humanities, Shaqra University, Ad-Dawadmi 11911, Saudi Arabia
[5]Department of Chemistry, Faculty of Science, Fayoum University, Fayoum City, Egypt

*Corresponding authors: E-mail: raj_rbm_raj@yahoo.co.in; aaalotaibi@su.edu.sa

Received: 14 February 2026 *Accepted*: 29 June 2026 *Published online*: 7 August 2026 AJC-22434

The constitution of the soft n-type magnesium ferrite in the hard cobalt ferrite nanoparticles was prepared using the hydrothermal chemical method and varied incrementally in a polyol-supported material. The $Mg_xCo_{1-x}Fe_2O_4$ nanoparticles exhibited uniform spherical morphology as observed in SEM analysis, while TEM confirmed well-dispersed particles with sizes ranging from 15 to 20 nm. Three phases of the material *viz*. $Mg_{0.1}Co_{0.9}Fe_2O_4$ (MCF101), $Mg_{0.3}Co_{0.7}Fe_2O_4$ (MCF103) and $Mg_{0.5}Co_{0.5}Fe_2O_4$ (MCF105) were prepared and utilised for the adsorption removal of methylene blue (MeB) dye from aqueous solution. The adsorption efficiency of 5 mg L^{-1} MeB ranged from 58-85% at pH 2.0, 50 min of stirring time and 1.0 g L^{-1} of adsorbent. Results indicated the gradual increase in Mg proportions has led to an enhancement in the removal efficiency in order MCF105, better than MCF103 and finally MCF101. Kinetic studies showed that the experimental results best matched the pseudo-second-order kinetics model and the film diffusion process was a rate-limiting phase. Equilibrium findings were well-fitted by the Langmuir isotherm model, with R^2 = 0.986-0.989 and maximal monolayer capacity (q_{max}) of 148-163 mg g^{-1}. The Freundlich isotherm analysis showed that the adsorption intensity parameter (n) exceeded unity for MCF103 and MCF105 confirmed favourable adsorption on these materials. MCF101, in contrast, exhibited behaviour characteristic of cooperative adsorption. The Temkin isotherm analysis indicated negligible lateral repulsive interactions among the adsorbed species.

Keywords: Magnesium-doped cobalt ferrite, Polyol-supported, Refinement Rietveld, Methylene blue, Adsorption.

INTRODUCTION

The conversion of hazardous and structurally complex dye molecules into less harmful and simpler compounds is referred to as dye degradation and is widely employed for the treatment of wastewater and contaminated environments [1-5]. The process plays a crucial role in mitigating environmental contamination and reducing potential risks to human health arising from the persistence and toxicity of synthetic dyes. Several methods such as chemical treatment, photocatalysis, biodegradation and adsorption have been explored for the removal of dyes [6,7].

Photocatalytic degradation involves the use of light responsive materials known as photocatalysts, which generate reactive oxidative species upon irradiation and facilitate the decomposition of dye molecules [8]. Among the photocatalysts investigated, zinc oxide (ZnO) and titanium dioxide (TiO_2) have received considerable attention because of their high activity and stability [9]. Biological degradation relies on the metabolic activity of microorganisms such as bacteria and fungi, which secrete enzymes capable of converting complex dye structures into simpler products [10]. Fungal enzymes such as laccase, manganese peroxidase and lignin peroxidase, exhibit high efficiency toward the degradation of azo dyes and related compounds. Chemical oxidation methods employ reagents like hydrogen peroxide, ozone and Fenton's reagent, which react with dye molecules and convert them into less toxic species [11].

Materials possessing high adsorption capacity, structural stability, regeneration ability and economic feasibility are

considered desirable for practical wastewater treatment applications [12-15]. Adsorption-based dye removal relies on materials capable of capturing dye molecules from aqueous solutions and separating them from the liquid phase. The adsorption efficiency is influenced by factors such as solution pH, initial dye concentration, contact time and the presence of competing ions or other dissolved species in the medium [16-18]. These considerations formed the basis for evaluating the adsorption performance of $Mg_xCo_{1-x}Fe_2O_4$ (x = 0.1, 0.3, 0.5) nanoferrites toward methylene blue removal.

$Mg_xCo_{1-x}Fe_2O_4$ (x = 0.1, 0.3, 0.5) ferrites were synthesised *via* the polyol method owing to its ability to produce nanoparticles with controlled particle size, morphology and composition. The method is cost-effective and minimises the possibility of contamination and harmful gaseous emissions commonly associated with several conventional solution-based synthesis routes. The prepared samples were characterised using various analytical techniques to examine their structural, morphological and functional properties. The adsorption behaviour of the prepared ferrites was investigated using methylene blue (MeB) dye as a model organic pollutant.

EXPERIMENTAL

All chemicals and reagents employed in this study were of analytical grade and were used without further purification. Cobalt nitrate hexahydrate [$Co(NO_3)_2{\cdot}6H_2O$; 99.5%], magnesium nitrate tetrahydrate [$Mg(NO_3)_2{\cdot}4H_2O$; 98.0%], iron nitrate nonahydrate [$Fe(NO_3)_3{\cdot}9H_2O$; 98.0%] and ethylene glycol (99.8%) were procured from CDH Ltd., India and used for the synthesis of ferrite nanoparticles. Methylene blue (MeB) dye was obtained from Fisher Chemicals (MA, USA). A stock solution (1%, w/v) was prepared in double-distilled water (DDW), from which a 5.0 mg L^{-1} working solution was obtained by appropriate dilution for adsorption experiments.

Characterization: The crystallographic properties and average crystallite size $Mg_xCo_{1-x}Fe_2O_4$ (x = 0.1, 0.3, 0.5) nanoferrites particles were investigated using an X-ray diffractometer (D8 Advance, Bruker, Germany). Fourier-transform infrared spectroscopy (Bruker, PN: 1010948106, Germany) was employed to examine the vibrational characteristics of the samples over the range of 4000-400 cm^{-1}. The surface morphology and particle characteristics were analysed using scanning electron microscopy (SEM, Carl Zeiss Sigma) and transmission electron microscopy (TEM, JEM-2010, JEOL, Japan), respectively. The concentration of MeB solutions was determined using a double-beam UV-Visible spectrophotometer (Cintra 1010, GBC Scientific Equipment) operated with Cintra 2.4 software at a wavelength of 664 nm. Solution pH was measured using a calibrated Jenway 4510 bench pH meter (Keison International Ltd., U.K.) with standard buffer solutions of pH 4 and 9. Agitation during adsorption experiments was provided by a Stuart S1500 orbital shaker (London, UK) operating within the range of 30-300 rpm. Double-distilled water obtained from a Hamilton purification system (Hamilton Glass Ltd., UK) was used throughout the experiments. Filtration was performed using qualitative filter paper No. 101 supplied by Dorsan Filtration SL Co. (Spain). Adsorption experiments were conducted in glass bottles sealed with Teflon-lined caps.

Synthesis of $Mg_xCo_{1-x}Fe_2O_4$ nanoparticles: $Mg_xCo_{1-x}Fe_2O_4$ (x = 0.1, 0.3 and 0.5) nanoferrites were synthesised by the polyol-assisted forced hydrolysis method using ethylene glycol as both solvent and reducing medium. The magnesium-to-cobalt molar ratios of 0.1:0.9, 0.3:0.7 and 0.5:0.5 yielded compositions designated as MCF101, MCF103 and MCF105, respectively. For MCF101, magnesium nitrate, cobalt nitrate and iron nitrate amounts of 0.2340 g, 2.3907 g and 7.3751 g were employed, respectively. The corresponding quantities for MCF103 were 0.7065 g, 1.8713 g and 7.4220 g, whereas MCF105 was prepared using 1.1800 g magnesium nitrate, 1.3420 g cobalt nitrate and 7.4690 g iron nitrate.

In brief, the metal precursors were dissolved separately in a mixture containing 25 mL of ethylene glycol and 25 mL of DDW under magnetic stirring until complete dissolution was achieved. The resulting solutions were refluxed at 90 ºC for 1 h. Sodium hydroxide solution (0.5 mol L^{-1}) was added dropwise to the reaction mixture until the pH approached 9.0, resulting in the formation of a precipitate. The reaction mixture was maintained under continuous stirring at 180 ºC for 4 h. After completion of the reflux process, the slurry was allowed to cool to room temperature. The precipitated product was washed repeatedly with ethanol and distilled water, dried at 90 °C and subsequently calcined at 400 ºC for 4 h to obtain the final ferrite nanoparticles.

RESULTS AND DISCUSSION

X-ray diffraction studies: The XRD patterns of $Mg_xCo_{1-x}Fe_2O_4$ (x = 0.1, 0.3, 0.5) nanoparticles are shown in Fig. 1. All diffraction peaks correspond to a single-phase cubic spinel ferrite structure with the face-centred cubic symmetry belonging to the $Fd\bar{3}m$ space group. The reflections indexed to the (220), (311), (222), (400), (422), (511) and (440) crystallographic planes agree well with the characteristic diffraction pattern of spinel ferrites. Increasing Mg^{2+} content decreases the peak broadening and improved peak sharpness, which is consistent with enhanced crystallinity and crystal growth.

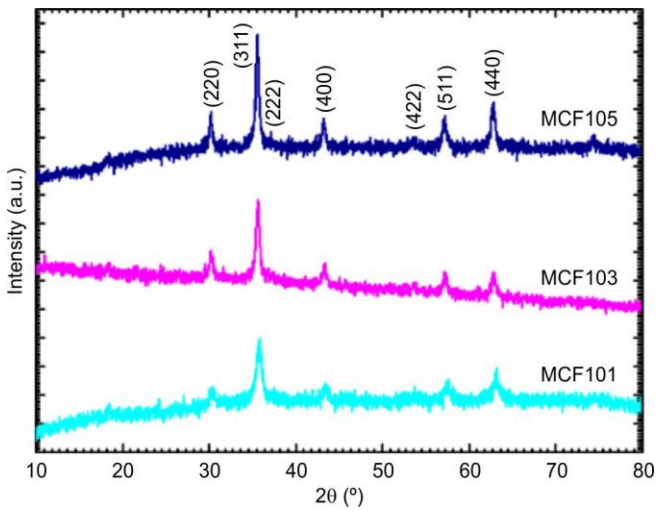

Fig. 1. XRD patterns of MCF101 ($Mg_xCo_{1-x}Fe_2O_4$, x = 0.1), MCF103 ($Mg_xCo_{1-x}Fe_2O_4$, x = 0.3) and MCF105 ($Mg_xCo_{1-x}Fe_2O_4$, x = 0.5) NPs

The Rietveld-refined diffraction profiles are shown in Fig. 2a. Refinement confirmed the formation of a cubic spinel structure belonging to the $Fd\bar{3}m$ space group. The low reliability factors (R-values) and goodness-of-fit values, listed in Table-1, established excellent agreement between the observed and calculated diffraction patterns, which confirmed phase purity, high crystallinity and structural homogeneity of the $Mg_xCo_{1-x}Fe_2O_4$ samples. The crystal structure of $Mg_{0.1}Co_{0.9}Fe_2O_4$ generated using the VESTA software package is shown in Fig. 2b.

The cation distribution derived from the Rietveld refinement results is summarized in Table-1. Increasing Mg^{2+} concentration promoted the migration of Co^{2+} ions from octahedral (B) sites to tetrahedral (A) sites, accompanied by the transfer of Fe^{3+} ions from A-sites to B-sites. This redistribution of cations confirms the partially inverse spinel nature of the prepared ferrites.

The lattice parameter and unit cell volume obtained from the refinement are also presented in Table-1. The lattice parameter increased from 8.3093 to 8.3577 Å with increasing Mg^{2+}

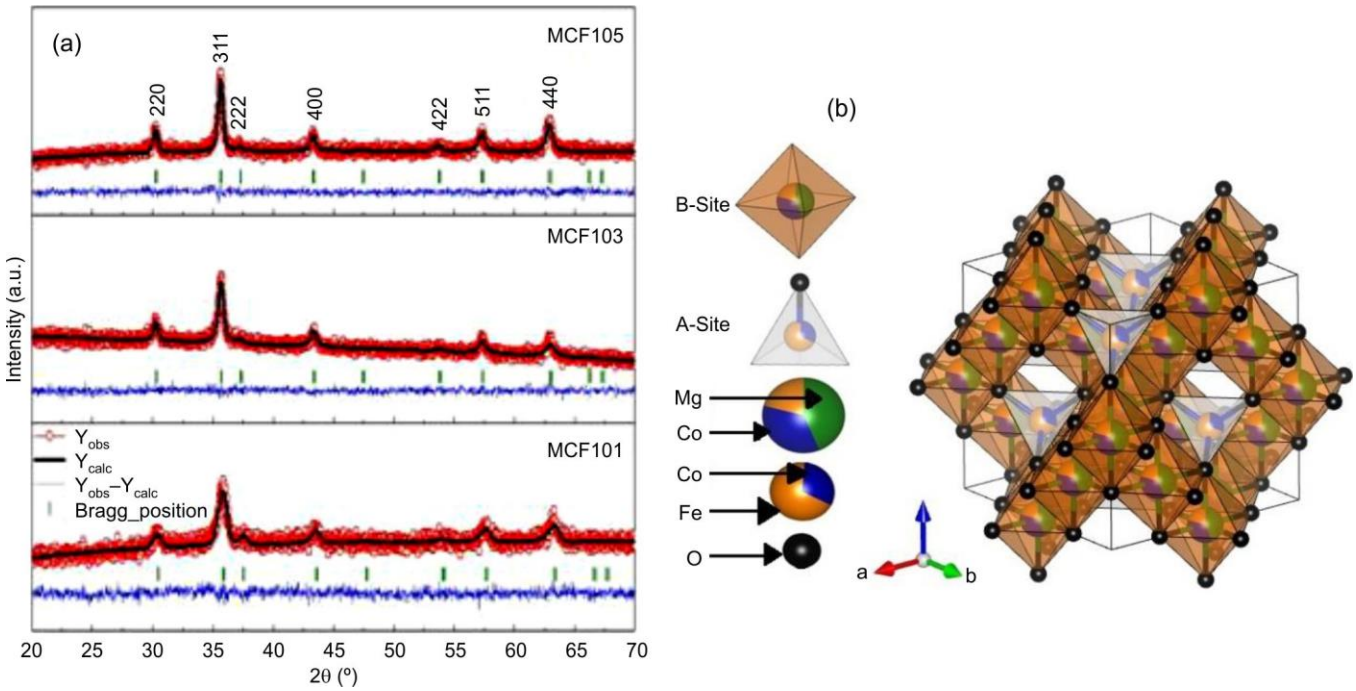

Fig. 2. (a) Rietveld refined XRD pattern of MCF101 ($Mg_xCo_{1-x}Fe_2O_4$, x = 0.1), MCF103 ($Mg_xCo_{1-x}Fe_2O_4$, x = 0.3) and MCF105 ($Mg_xCo_{1-x}Fe_2O_4$, x = 0.5) and (b) polyhedron of face-centered cubic spinel structure of MCF101 ($Mg_{0.1}Co_{0.3}Fe_2O_4$) sample

TABLE-1
SUMMARY OF THE REFINEMENT RIETVELD ANALYSIS, INCLUDING THE RELIABILITY FACTORS (R_p, R_{wp}, R_{exp} AND χ^2), CATION OCCUPANCY IN A- AND B-SITES, LATTICE PARAMETER (a), UNIT CELL VOLUME (V), MEAN CRYSTALLITE SIZE (D), MICROSTRAIN (ε), X-RAY DENSITY (ρ_{xr}d) AND DISLOCATION DENSITY (δ), SPECIFIC SURFACE AREA (S.A) AND OXYGEN POSITIONAL PARAMETER ($u^{\bar{4}3m}$) FOR $Mg_xCo_{1-x}Fe_2O_4$ (x = 0.1, 0.3, 0.5) NANOPARTICLES

Parameters	MCF 101	MCF103	MCF105
Refinement factors:			
R_p	3.04	3.64	3.12
R_{wp}	3.80	4.60	3.96
R_{exp}	3.62	4.48	3.89
χ^2	1.11	1.05	1.04
Cation distribution:			
A-Site	$(Co_{0.30380}Fe_{0.69620})$	$(Mg_{0.06838}Co_{0.35043}Fe_{0.58120})$	$(Mg_{0.27736}Co_{0.27372}Fe_{0.44892})$
B-Site	$[Mg_{0.1}Co_{0.59620}Fe_{1.30380}]$	$[Mg_{0.23162}Co_{0.34957}Fe_{1.41880}]$	$[Mg_{0.22264}Co_{0.22628}Fe_{1.55108}]$
The refined crystal data:			
a (Å)	8.3093	8.3506	8.3577
V (Å^3)	573.721	582.301	583.791
ρ_{xrd} (g/cm^3)	5.3516	5.1147	4.9441
D (nm)	11.67	33.10	23.16
ε	1.749×10^{-3}	3.155×10^{-3}	1.302×10^{-3}
δ (nm^{-2})	7.34×10^{-3}	9.13×10^{-4}	1.86×10^{-3}
S.A (cm^2/g)	1.13×10^{6}	6.64×10^{5}	5.92×10^{5}
$u^{\bar{4}3m}$ (Å)	0.37895	0.38790	0.37508

concentration owing to lattice expansion caused by the Mg^{2+} substitution. Similar behaviour has been reported for Mg-substituted cobalt ferrites [19].

The oxygen positional parameter ($u^{\bar{4}3m}$) obtained from the refinement is also shown in Table-1. This parameter is strongly influenced by synthesis conditions, thermal treatment and chemical composition. For an ideal spinel structure with the origin located at the tetrahedral site, the oxygen positional parameter assumes a value of ($u^{\bar{4}3m}$) = 0.375, which is consistent to ideal cubic close packing of oxygen ions. The higher values observed in the present study arise from the displacement of O^{2-} ions along the (111) directions away from the tetrahedral cations. Such displacement leads to expansion of the tetrahedral interstices accompanied by contraction of the octahedral sites within the spinel lattice [20].

The X-ray density (ρ_{xrd}) was computed using eqn. 1 and its values (Table-1) decreased with increasing Mg^{2+} concentration owing to the combined effect of lower molecular weight and larger lattice parameter.

$$\rho_{xrd} = \frac{8M}{Na^3} \quad (1)$$

The Williamson-Hall (W-H) method [21] was employed to evaluate the combined contributions of crystallite size and lattice strain to peak broadening, providing additional microstructural information beyond that obtained from the Scherrer equation. The method separates the size- and strain-induced broadening components through the relationship given in eqn. 2. Crystallite size was obtained from the *y*-intercept of the $\beta_{hkl}\cos\theta$ *versus* $4\sin\theta$ plot, whereas lattice strain was determined from the slope of the fitted line. The calculated values are listed in Table-1 and the corresponding W-H plots for the $Mg_xCo_{1-x}Fe_2O_4$ samples are presented in Fig. 3.

$$\beta\cos\theta = \frac{K\lambda}{D} + 4\varepsilon\sin\theta \quad (2)$$

where K (0.94) represents the shape constant, λ is the X-ray wavelength, β denotes the full width at half maximum (FWHM)

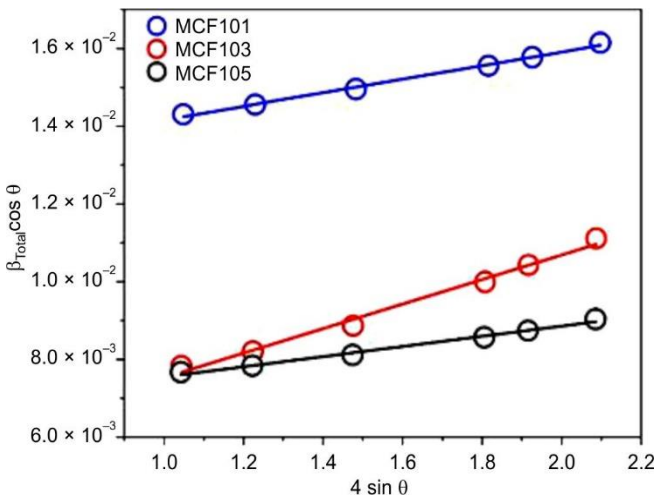

Fig. 3. Williamson-Hall plots of MCF101 ($Mg_xCo_{1-x}Fe_2O_4$, x = 0.1), MCF103 ($Mg_xCo_{1-x}Fe_2O_4$, x = 0.3) and MCF105 ($Mg_xCo_{1-x}Fe_2O_4$, x = 0.5) NPs

of six selected peaks, ε corresponds to the lattice strain and θ is the Bragg diffraction angle.

The estimated crystallite sizes varied from 11.67 to 33.10 nm and did not follow a regular trend with increasing Mg^{2+} concentration. This behaviour may arise from differences in the synthesis conditions (i), changes in lattice distortion and internal stress associated with the increase in lattice parameter after Mg^{2+} substitution (ii), and variations in the bond energies of metal–oxygen and Fe–O bonds, which influence crystallite growth during synthesis (iii) [22,23]. The positive slope obtained from the Williamson-Hall plots confirms the presence of tensile lattice strain in the prepared samples.

Tensile strain is indicated by a positive slope value:

$$\delta = \frac{1}{D^2} \quad (3)$$

The specific surface area (S.A.) was estimated using eqn. 4 to evaluate the defect level in the synthesized nanoferrites [24], where D and $\rho_{xr}d$ correspond to the crystallite size and X-ray density, respectively. A reduction in specific surface area was observed with increasing Mg^{2+} content due to crystallite growth.

$$\text{S.A.} = \frac{6}{(D\times\rho_{xrd})} \quad (4)$$

Based on the estimated oxygen positional parameter, the experimentally obtained lattice constant (a) and the ionic radius of oxygen (R_o = 1.38 Å), the geometrical parameters are as follows:

Tetrahedral bond length (d_{AO}), octahedral bond length (d_{BO}), tetrahedral edge length (d_{AE}), shared octahedral edge length (d_{BE}) and unshared octahedral edge length (d_{BEU}) for $Mg_xCo_{1-x}Fe_2O_4$ (x = 0.1, 0.3, 0.5) nanoferrites were calculated using eqns. 5-9 [25,26]. The resulting values are summarised in Table-2.

$$d_{AO} = a_{exp}\sqrt{3}\left(u^{\bar{4}3m} - 0.25\right) \quad (5)$$

$$d_{BO} = a_{exp}\left(3(u^{\bar{4}3m})^2 - \frac{11}{4}(u^{\bar{4}3m}) + \frac{43}{64}\right)^{1/2} \quad (6)$$

$$d_{AE} = a_{exp}\sqrt{2}\left(2u^{\bar{4}3m} - 0.5\right) \quad (7)$$

$$d_{BE} = a_{exp}\sqrt{2}\left(1 - 2u^{\bar{4}3m}\right) \quad (8)$$

$$d_{BEU} = a_{exp}\left(4(u^{\bar{4}3m})^2 - 3(u^{\bar{4}3m}) + \frac{11}{16}\right)^{1/2} \quad (9)$$

Table-2 shows that the tetrahedral bond lengths (d_{AO} and d_{AE}) increased up to x = 0.3 and decreased at x = 0.5. An opposite trend was observed for the octahedral bond lengths (d_{BO} and d_{BE}), which decreased at x = 0.3 and increased at x = 0.5. The increase in d_{BEU} with Mg^{2+} concentration is associated with the redistribution of cations between the tetrahedral and octahedral sites.

Theoretical calculations of the tetrahedral (r_{Td}) and octahedral (r_{Oct}) ionic radii for all synthesised samples were performed using eqns. 10 and 11 [27] and the obtained values are shown in Table-2.

TABLE-2
CALCULATED VALUES OF d_{AE}, d_{BE}, d_{BEU}, d_{AO}, d_{BO}, r_A AND r_B FOR $Mg_xCo_{1-x}Fe_2O_4$ (x = 0.1,0.3,0.5) NANOPARTICLES

Sample	d_{AO} (Å)	d_{BO} (Å)	d_{AE} (Å)	d_{BE} (Å)	d_{BEU} (Å)	r_A (Å)	r_B (Å)
MCF101	1.8559	2.0450	3.0306	2.8449	2.9385	0.51734	0.67856
MCF103	1.9945	1.9858	3.2571	2.6477	2.9602	0.52701	0.67116
MCF105	1.8107	2.0888	2.9568	2.9530	2.9549	0.53682	0.66466

$$r_{Td} = \left(C^{A}_{Mg^{2+}}\right)\left(r^{A}_{Mg^{2+}}\right) + \left(C^{A}_{Co^{2+}}\right)\left(r^{A}_{Co^{2+}}\right) + \left(C^{A}_{Fe^{3+}}\right)\left(r^{A}_{Fe^{3+}}\right) \quad (10)$$

$$r_{Oct} = \frac{1}{2}\left[\left(C^{B}_{Mg^{2+}}\right)\left(r^{B}_{Mg^{2+}}\right) + \left(C^{B}_{Co^{2+}}\right)\left(r^{B}_{Co^{2+}}\right) + \left(C^{B}_{Fe^{3+}}\right)\left(r^{B}_{Fe^{3+}}\right)\right] \quad (11)$$

where C^A are the ionic concentrations for A-sites and C^B for B-sites, respectively, $r_{Mg^{2+}}$, $r_{Co^{2+}}$ and $r_{Fe^{3+}}$ are radii of Mg^{2+}, Co^{2+} and Fe^{3+} ions, respectively. The value of r_B decrease with increasing Mg^{2+} substation while r_A increasing. The decrease in r_B is due to a decrease in Co^{2+} in B-sites with larger ionic radii (0.745 Å) and an increase in Mg^{2+} in A-sites with lower ionic radii (0.72 Å). Furthermore, the interionic distances between cation-anion (p, q, r, s) and between cation-cation (b, c, d, e, f) were evaluated by eqns. 12-20 [28] and the obtained values are listed in Table-3.

For A-A interaction:

$$d = \frac{a\sqrt{3}}{4} \quad (12)$$

For B-B interaction:

$$b = \frac{a\sqrt{2}}{4} \quad (13)$$

For B-B interaction:

$$f = \frac{a\sqrt{6}}{4} \quad (14)$$

For A-B interaction:

$$e = \frac{a3\sqrt{3}}{8} \quad (15)$$

For A-B interaction:

$$c = \frac{a\sqrt{11}}{8} \quad (16)$$

For A-O interaction:

$$q = a\sqrt{3}\left(u^{\bar{4}3m} - \frac{1}{4}\right) \quad (17)$$

For A-O interaction:

$$r = a\left(u^{\bar{4}3m} - \frac{1}{4}\right)\sqrt{11} \quad (18)$$

For B-O interaction:

$$p = a\left(\frac{5}{8} - u^{\bar{4}3m}\right) \quad (19)$$

For B-O interaction:

$$s = a\left(\frac{u^{\bar{4}3m}}{3} + \frac{1}{8}\right)\sqrt{3} \quad (20)$$

The interatomic distance of cations (d, b, f, e, and c) depictsan increasing trend with increasing Mg^{2+} substitution. These changes in (d, b, f, e and c) result from the arrangement of ions of varying sizes in various sub-lattices, which altered the cationic interatomic distance. The interatomic distance of cation-anion (q, r, s) shows an increasing trend when x = 0.3, except for (p), however, the trend changes inversely for x = 0.5.

Moreover, the bond angles (θ_1, θ_2, θ_3, θ_4, θ_5) among ion pairs were evaluated using eqns. 21-25 [8] and the obtained values are reported in Table-4.

For A-A interaction:

$$\theta_5 = \cos^{-1}\left(\frac{r^2 + q^2 - d^2}{2qr}\right) \quad (21)$$

For B-B interaction:

TABLE-3
VALUES OF INTERIONIC DISTANCE FOR MCF101 ($Mg_xCo_{1-x}Fe_2O_4$, x = 0.1), MCF103 ($Mg_xCo_{1-x}Fe_2O_4$, x = 0.3) AND MCF105 ($Mg_xCo_{1-x}Fe_2O_4$, x = 0.5) NPs

Sample	Cation-cation (Å)					Cation-anion (Å)			
	d	b	f	e	c	q	r	p	s
MCF101	3.59803	2.93778	5.08839	5.39705	3.44485	1.85587	3.55371	2.04450	3.61698
MCF103	3.61592	2.95238	5.11368	5.42387	3.46198	1.99454	3.81925	1.97993	3.67811
MCF105	3.61899	2.95489	5.11803	5.42849	3.46492	1.81065	3.46714	2.08876	3.61938

TABLE-4
VALUES OF INTERIONIC ANGLES (º) FOR MCF101 ($Mg_xCo_{1-x}Fe_2O_4$, x = 0.1), MCF103 ($Mg_xCo_{1-x}Fe_2O_4$, x = 0.3) AND MCF105 ($Mg_xCo_{1-x}Fe_2O_4$, x = 0.5) NPs

Sample	Bond angle (º)				
	θ_1	θ_2	θ_3	θ_4	θ_5
MCF101	123.99337	147.97148	91.85470	125.69345	76.28539
MCF103	121.16233	136.17778	96.41765	126.68437	68.87837
MCF105	125.23846	154.60549	90.03669	125.27303	79.89729

$$\theta_3 = \cos^{-1}\left(\frac{2p^2 - b^2}{2p^2}\right) \quad (22)$$

For B-B interaction:

$$\theta_4 = \cos^{-1}\left(\frac{p^2 + s^2 - f^2}{2ps}\right) \quad (23)$$

For A-B interaction:

$$\theta_2 = \cos^{-1}\left(\frac{p^2 + r^2 - e^2}{2pr}\right) \quad (24)$$

For A-B interaction:

$$\theta_1 = \cos^{-1}\left(\frac{p^2 + q^2 - c^2}{2pq}\right) \quad (25)$$

In an undistorted spinel structure, the A-O-B angles are around 125º and 154º. One of the B-O lengths is significant in the latter, yet the B-O-B angles are 90º and 125º. For the A–A case, the angle is almost 80º. As a result, the strongest exchange interactions occur between A and B. Furthermore, the B-B interactions are significantly weaker and the A–A interactions are the most unfavourable situation that occurs [29].

The interaction of A-A and A-B is dependent on θ_1, θ_2 and θ_5, whereas the B-B interaction changes with θ_3 and θ_4. The interionic angles θ_1, θ_2 and θ_5 decreased up to x = 0.3, whereas θ_3 and θ_4 increased. At x = 0.5, the interionic angles exhibited the opposite behaviour, with θ_1, θ_2 and θ_5 increasing and θ_3 and θ_4 decreasing. Since the magnetic properties of spinel ferrite structures are affected by the cation interaction of the A- and B-sites, therefore, this variation has a high effect on the net magnetic moment of the samples. Increasing (θ_1, θ_2 and θ_5) and decreasing (θ_3 and θ_4) indicate strong A-A and A-B interactions and weak B-B interactions, respectively.

FT-IR study: FTIR spectra of $Mg_xCo_{1-x}Fe_2O_4$ (x = 0.1, 0.3, 0.5) nanoferrites synthesised *via* the polyol method exhibit strong characteristic bands at 597 cm^{-1} due to the Mg-O bond stretching vibrations, which increased by increasing Mg content. The two weak spinel ferrite bands at 471 cm^{-1} (tetrahedral) and 483 cm^{-1} (octahedral) are due to the stretching vibrations of Co-O and Fe-O bonds, respectively. The increase in the intensity of the Fe–O band with Mg content is attributed to the migration of Fe^{3+} ions towards the octahedral (B) sites accompanied by the transfer of Co^{2+} ions to the tetrahedral (A) sites during Mg substitution. Additional peaks at 1128 and 1383 cm^{-1} correspond to C–O and C–H vibrations, while 1633 and 3406 cm^{-1} indicate surface –OH groups and adsorbed moisture. The 2923 cm^{-1} band arises from $–CH_2$ stretching, which is attributed due to the presence of the residual organics aroused from the polyol medium (Fig. 4).

Morphological studies: The surface morphology of the synthesized MCF101, MCF103 and MCF105 nanoferrites was examined by SEM. The SEM images (5a-c) show nearly spherical particles with a fairly uniform distribution, which confirmed the formation of the ferrite phase. Grain size distributions (Fig. 5d-f) reveal average particle sizes in the range of 0.095-0.252 μm with relatively narrow size distributions. The average grain size decreased with increasing Mg content,

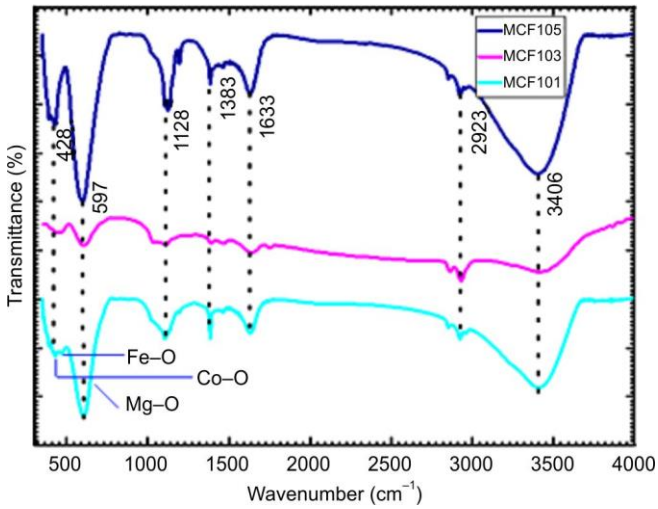

Fig. 4. FTIR spectra of MCF101 ($Mg_xCo_{1-x}Fe_2O_4$, x = 0.1), MCF103 ($Mg_xCo_{1-x}Fe_2O_4$, x = 0.3) and MCF105 ($Mg_xCo_{1-x}Fe_2O_4$, x = 0.5) NPs

following the order MCF101 > MCF103 > MCF105, which highlights the influence of the Mg/Co precursor ratio on the particle growth.

Transmission electron microscopy (TEM) micrographs (Fig. 6a-c) confirm the nearly spherical morphology and nanocrystalline nature of the prepared ferrites. Particle size distributions and the corresponding histograms are shown in Fig. 6d-f. The average particle sizes were found to lie in the range of 29-39 nm. A gradual reduction in particle size was observed with increasing Mg content, which may be associated with lattice distortion and strain arising from the larger ionic radius of Mg^{2+} compared with Co^{2+}, thereby restricting further particle growth.

Adsorption study

The concentration of MeB dye was analysed at a wavelength of 665 nm *via* a UV-Visible spectrophotometer. A magnetic stirrer with a hotplate was utilised to agitate the samples at around 500 rpm at a speed of 250 rpm. For the adsorption study, 50 mL glass bottles with Teflon-lined caps were employed. Decolouration of MeB dye was investigated using a 50 mL solution with 5 mg L^{-1} of the aqueous dye solution and 0.05 g of adsorbent under magnetic stirring for 5-60 min at room temperature. Following treatment, the adsorbent was separated magnetically and residual dye concentration was measured spectrophotometrically. A calibration curve was obtained from the absorbance values of MeB dye standard solutions in the concentration range of 0-20 mg L^{-1} at the maximum absorption wavelength of 665 nm. The resulting calibration equation was A = 0.073C + 0.026 with a correlation coefficient (R^2) of 0.998. For C_o representing the initial and C_e, respectively. The removal of MeB dye was measured according to eqn. 26:

$$\text{Removal (\%)} = \frac{C_o - C}{C_o} \times 100 \quad (26)$$

Moreover, eqn. 27 was employed to estimate the equilibrium amount of MeB dye molecules adsorbed per gram of adsorbent (q_e, mg g^{-1}).

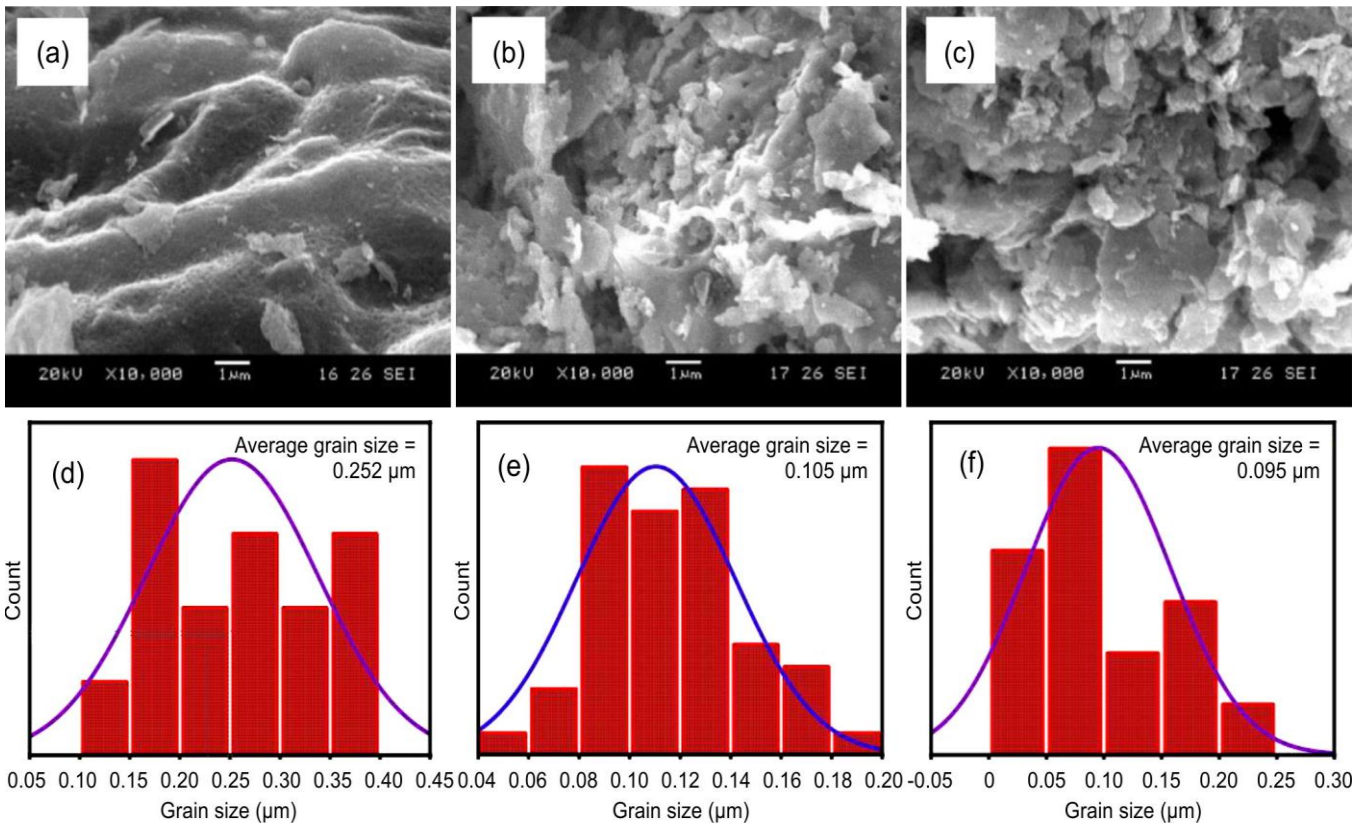

Fig. 5. The SEM images of MCF101 (a), MCF103 (b) and MCF105 (c) NPs, respectively. Histograms of the grain size distribution for MCF101 (d), MCF103 (e) and MCF105 (f)

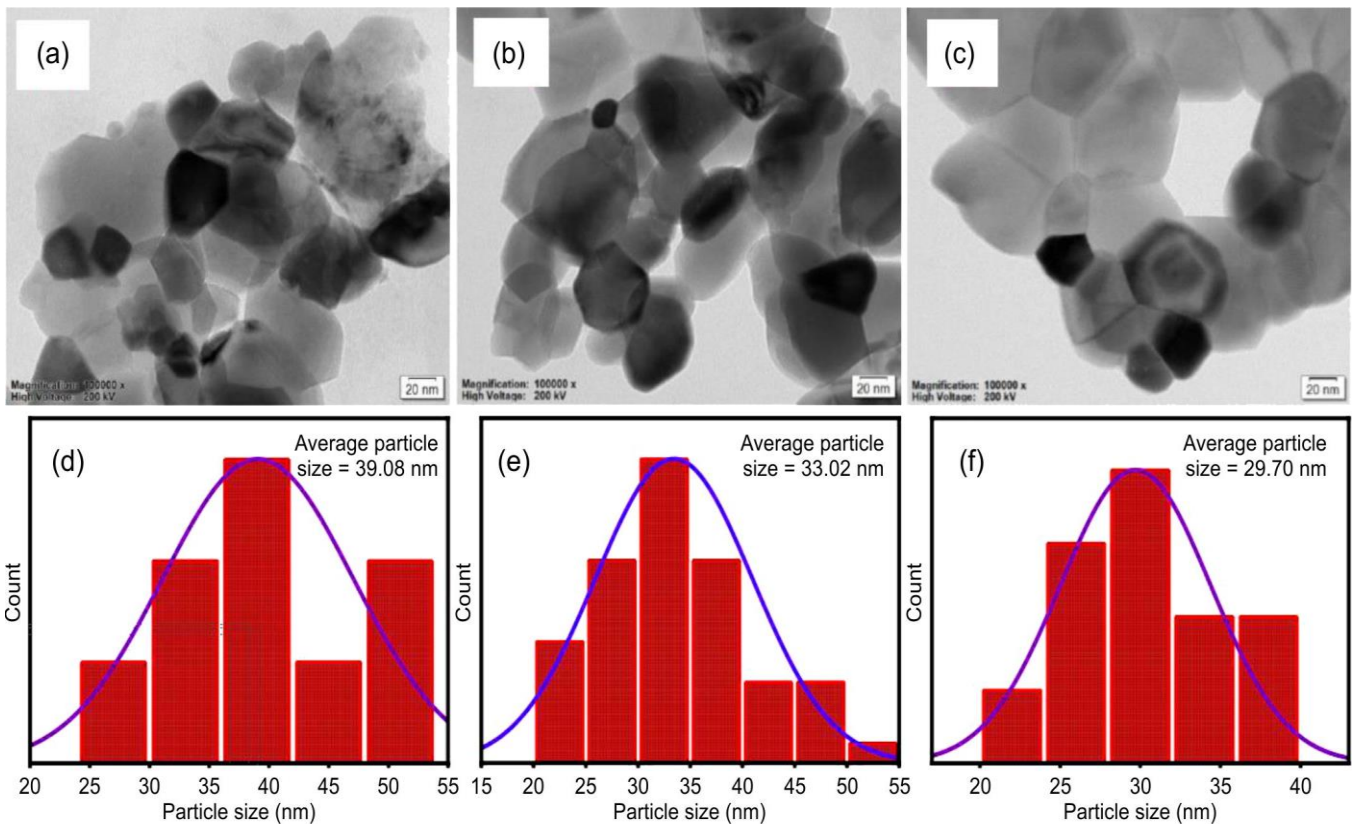

Fig. 6. The TEM images of MCF101 (a), MCF103 (b) and MCF105 (c) NPs, respectively. The particle size distribution histograms for MCF101 (d), MCF103 (e) and MCF105 (f)

$$q_e = \frac{(C_o - C) \times V}{m} \quad (27)$$

Adsorption performance

Effect of pH: The pH of the solution influences both the ionic state of the MeB dye and the surface charge characteristics of the $Mg_xCo_{1-x}Fe_2O_4$/polyol nanoferrites, thereby playing a crucial role in determining the adsorption behaviour. The effect of solution pH on MeB removal by the synthesized nanoferrites is shown in Fig. 7 using an initial dye concentration of 5 mg L^{-1}. Since MeB is a cationic dye, its adsorption is strongly influenced by the surface charge of the adsorbent. MCF101 exhibited a gradual increase in removal efficiency from 44% at pH 2 to 58% at pH 8, followed by a slight decrease at higher pH values. MCF103 and MCF105 maintained comparatively high removal efficiencies over a broad pH range (2-7), reaching approximately 74% and 82%, respectively, before decreasing slightly in alkaline media (pH 8-10).

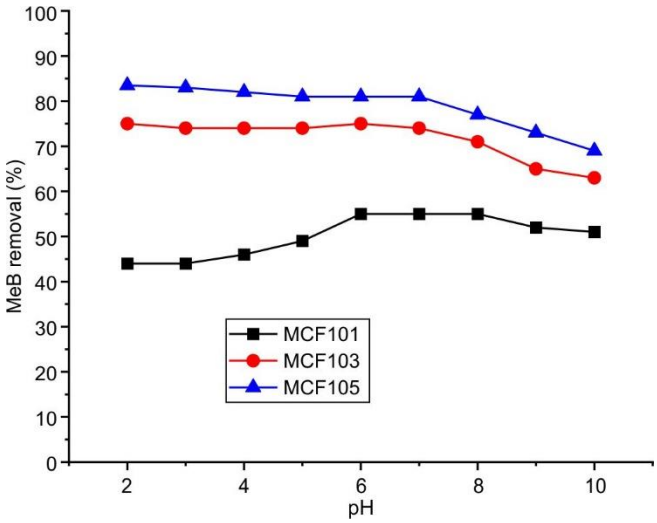

Fig. 7. Effect of pH on the MeB adsorption onto MCF101 ($Mg_xCo_{1-x}Fe_2O_4$, x = 0.1), MCF103 ($Mg_xCo_{1-x}Fe_2O_4$, x = 0.3) and MCF105 ($Mg_xCo_{1-x}Fe_2O_4$, x = 0.5)/polyol materials (5 mg L^{-1}), sample volume of 50 mL, 60 min stirring time and adsorbent weight 0.05 g

The adsorption behaviour can be interpreted in terms of the point of zero charge (pH_{pzc}), which governs the surface charge of nanoferrite materials. Magnesium nanoferrite-based adsorbents generally possess pH_{pzc} values between 5.0 and 6.6, depending on composition, synthesis route, surface modification and calcination temperature, whereas polyol functionalisation may shift the pH_{pzc} towards lower values [30]. Under acidic conditions, hydrogen bonding contributes significantly to dye uptake, while electrostatic attraction becomes increasingly important at pH values above the pH_{pzc}. The higher adsorption capacity of MCF103 and MCF105 is attributed to the higher abundance of negatively charged Mg–O surface groups, which enhance the interaction with positively charged MeB molecules.

A slight reduction in removal efficiency above pH 8 was observed for all samples, which may be associated with the changes in dye speciation and surface interactions under alkaline conditions [31]. The adsorption performance followed the order $Mg_{0.5}Co_{0.5}Fe_2O_4$ > $Mg_{0.3}Co_{0.7}Fe_2O_4$ > $Mg_{0.1}Co_{0.9}Fe_2O_4$, which confirmed the beneficial role of Mg incorporation in dye removal. Electrostatic interactions and hydrogen bonding appear to be the dominant adsorption mechanisms since the nanoferrite structure lacks aromatic groups capable of participating in π-π interactions. Although MCF103 and MCF105 exhibited their highest removal efficiencies at pH 2, practical wastewater treatment processes are generally conducted near neutral pH. The variation in removal efficiency between pH 2 and 7 remained within ±10%, demonstrating the suitability of these materials over a wide pH range. Consequently, pH 6.5 was selected as the optimum operating condition for subsequent adsorption experiments.

Adsorption kinetics: The effect of contact time on MeB adsorption by $Mg_xCo_{1-x}Fe_2O_4$/polyol materials was investigated over the range of 2-100 min and the corresponding adsorption profiles (q_t *versus* time) are shown in Fig. 8. The adsorption capacity increased rapidly during the initial stages of the process and followed the order MCF105 > MCF103 > MCF101 throughout the investigated period. Despite the differences in adsorption capacity, all samples attained equilibrium within 40 min. The rapid initial uptake is attributed to the availability of a large number of active adsorption sites on the adsorbent surface, followed by a slower approach to equilibrium as these sites became progressively occupied. Diffusion of MeB molecules from the bulk solution to the adsorbent surface also contributes to the adsorption rate. Distinct differences in adsorption affinity among the three materials were evident during the early stages of adsorption. After 5 min of contact time, the adsorption capacities reached 2.0, 4.5 and 5.3 mg g^{-1} for MCF101, MCF103 and MCF105, respectively. The equilibrium adsorption capacities were 5.3, 8.4 and 9.6 mg g^{-1} for MCF101, MCF103 and MCF105, respectively. A contact time of 60 min was selected for subsequent experiments to ensure complete equilibration.

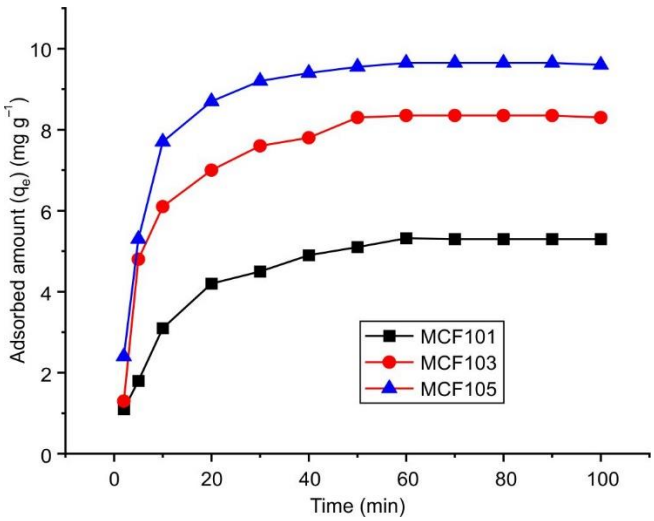

Fig. 8. Influence of stirring time on MeB adsorption by $Mg_xCo_{1-x}Fe_2O_4$/polyol nanocomposites (5 mg L^{-1}, 50 mL, 0.05 g adsorbent, 100 min)

To identify the main rate-controlling mechanism, the pseudo-first- order, second-order and intra-particle model of diffusion were applied to the experimental information in order to investigate the adsorption kinetics. Here, q_e and q_t

represent the amounts of MeB adsorbed (mg g^{-1}) at equilibrium and at any given time t (min), respectively. According to Ho & McKay [32], the pseudo-first-order kinetic model can be expressed as shown in eqn. 28:

$$\log(q_e - q_t) = \log q_e - \frac{k_1 t}{2.303} \quad (28)$$

The linear relationship between log ($q_e - q_t$) and time can be employed to evaluate whether the pseudo-first-order kinetic model appropriately describes the system.

In addition, Ho *et al.* [33] formulated the pseudo-second-order kinetic expression as shown in eqn. 29:

$$\frac{t}{q_t} = \frac{1}{K_2 q_e^2} + \frac{1}{q_e} t \quad (29)$$

where k_2 is the pseudo-second order rate constant (mg g^{-1} min^{-1}).

Fig. 9a-b shows plots of the two examined models. Table-5 compiles the resulting kinetic parameter data. A comparison of the values of the correlation coefficient (R^2) obtained from the regression analysis revealed that a higher value was attained for the pseudo-second-order model than for the pseudo-first-order model. Therefore, the pseudo-second-order model was recognised as the best fit for the experimental results and was more representative for describing the findings. Accordingly, the adsorption process followed pseudo-second-order kinetic behaviour and based on this conclusion, the features of both the dye and adsorbent surface groups would control the adsorption kinetics. Moreover, the calculated q_e values for all materials MCF101, MCF103 and MCF105 were very close to the experimental value. Further, the second-order rate constant (K_2) was in the order MCF105 > MCF103 > MCF101 indicated the increase in adsorption efficiency by increasing Mg content, which might be due to a further increase in adsorption processing.

The Morris–Weber model [34] describes the intra-particle diffusion behaviour of the adsorption process. Plotting q_t values *versus* $t^{0.5}$ enables the computation of the intra-particle diffusion rate constant k_{id} (mg g^{-1} $min^{-1/2}$), as derived from the slope of eqn. 30.

$$q_t = k_{id} t^{0.5} \quad (30)$$

The intra-particle diffusion plots obtained over the studied contact time range are shown in Fig. 9c. Linear relationships with correlation coefficients ranging from 0.938 to 0.986 were obtained for all samples. The adsorption profiles consisted of distinct linear regions with different slopes, which indicates that the adsorption process proceeded through multiple stages rather than a single diffusion step. The initial region with a steeper slope corresponds to the rapid transfer of MeB molecules from the bulk solution to the external adsorbent surface through film diffusion, whereas the later stage is associated with intra-particle diffusion within the adsorbent pores. The deviation of the linear plots from the origin confirms that intra-particle diffusion was not the sole rate-controlling mechanism and that film diffusion also contributed to the overall adsorption process. The values of K_{id} ranged from 0.288 to 0.889 mg g^{-1} $min^{-1/2}$ in the order MCF101 > MCF103 > MCF105, which confirmed that the MCF101 material was the most influenced by the diffusion process, while MCF105 was the least influenced. This may explain the fast adsorption kinetics of MCF105, which might have more accessible surface groups to attract the dye strongly from the bulk solution, rather than MCF101. The MCF103 material showed intermediate behaviour, which could be a result of the moderate Mg content. Thus, it could be interpreted that increasing the proportion of Mg in the material has a determinant effect on reducing the diffusion control of adsorption. The intraparticle diffusion behaviour was not effective for these adsorbents, which might be due to

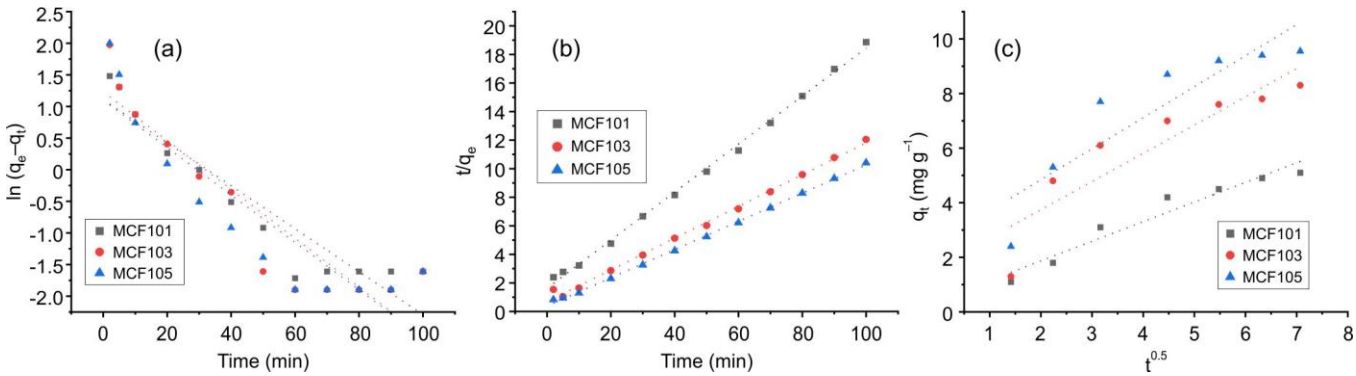

Fig. 9. (a) Pseudo-first order kinetic model, (b) pseudo-second order kinetic model and (c) intra-particle diffusion model for adsorption of MeB dye (5 mg L^{-1}), pH 6.5, 0.05 g adsorbent

TABLE-5
ADSORPTION KINETIC DATA FOR MeB DYE ADSORPTION ONTO $Mg_xCo_{1-x}Fe_2O_4$/POLYOL MATERIALS

Adsorbent	Pseudo-first-order model				Pseudo-second-order model			Intra-particle diffusion	
	$q_{e,\ exp.}$ (mg g^{-1})	q_e (mg g^{-1})	K_1 (min^{-1})	R^2	q_e (mg g^{-1})	K_2 (g mg^{-1} min^{-1})	R^2	K_{id} (mg^{-1} g $min^{1/2}$)	R^2
MCF101	5.3	1.54	0.0340	0.875	5.9	0.0173	0.998	0.719	0.932
MCF103	8.4	3.45	0.0386	0.839	8.9	0.0181	0.996	1.033	0.778
MCF105	9.6	3.01	0.0374	0.791	10.1	0.0255	0.999	1.136	0.775

the large MeB molecules not transferring within the adsorbent micropores and thus not being affected by different intermolecular repellent forces. Thus, the adsorption kinetics of MeB dye molecules are expected to be controlled by both pseudo-second-order and film diffusion-controlled models.

Adsorption equilibrium: Equilibrium experiments were conducted using model MeB solutions with an initial concentration ranging from 2 to 100 mg L^{-1} adjusted to pH 2 and a stirring time of 50 min. The adsorption isotherms are shown in Fig. 10. The maximum experimental adsorption capacity for MeB ranged from 148 to 163 mg g^{-1}. The equilibrium or remaining concentration (C_e, mg L^{-1}) was distant lower than the initial concentration (C_o, mg L^{-1}) at low levels of MeB, whereas at higher levels, the C_e value increased as the adsorbent became near saturation and exceeded the equilibrium adsorption capacity. When the C_o concentration reached 70 mg L^{-1}, the isotherm reached a leveling-off segment corresponding to the maximum experimental adsorption capacity, $q_{max,\ exp}$.

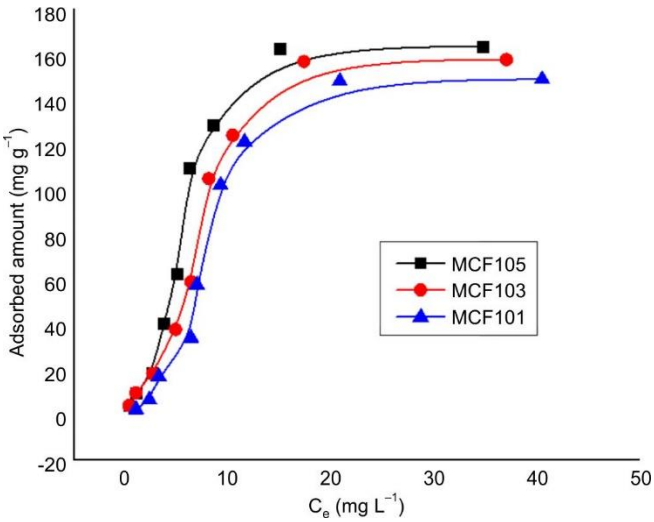

Fig. 10. Equilibrium isotherm of MeB adsorption to $Mg_xCo_{1-x}Fe_2O_4$/polyol materials using a concentration ranging from 2-100 mg L^{-1}, pH 2, sample volume of 50 mL, adsorbent weight 0.05 g and stirring time of 50 min

To estimate the adsorption isotherm parameters, the equilibrium data were linearised using the linearised forms of Freundlich, Langmuir and Temkin models. The Langmuir isotherm [35] is given by eqn. 31:

$$\frac{C_e}{q_e} = \frac{C_e}{q_{max}} + \frac{1}{q_{max}K_L} \quad (31)$$

whereas q_e (mg g^{-1}) is the equilibrium amount adsorbed for MeB, q_{max}, (mg g^{-1}) is the maximum adsorption capacity for a monolayer and C_e (mg L^{-1}) is the equilibrium concentration of MeB. K_L is the Langmuir constant, which is a measure of the binding sites' affinity for MeB. A good agreement between the experimental data and the model indicates that adsorption proceeded predominantly through a monolayer chemisorption mechanism. The model further makes it possible for the calculation of q_{max} and dimensionless separation factor R_L (eqn. 32), which can be used to predict favourable adsorption:

$$R_L = \frac{1}{1+K_L C_e} \quad (32)$$

The Freundlich isotherm [36], which describes adsorption on actively heterogeneous surfaces, is represented by eqn. 33:

$$\ln q_e = \left(\frac{1}{n}\right)\ln C_e + \ln K_F \quad (33)$$

where K_F and n denote the constants corresponding to the adsorption capacity and the adsorption intensity.

The Temkin isotherm model [37] is employed to assess the interaction among the adsorbent and the adsorbate, along with corresponding heat of adsorption. It is expressed by eqn. 34:

$$q_e = B\ln A_T + B\ln C_e \quad (34)$$

where A_T (L g^{-1}) denotes the Temkin equilibrium binding constant and B is the slope.

The parameter (b_T), referred to as the Temkin constant, is directly related to the adsorption heat (J mol^{-1}) and is calculated using eqn. 35. The temperature-dependent isotherm constant, linked to the heat of adsorption (J mol^{-1}) as described in eqn. 35:

$$B = \frac{RT}{b_T} \quad (35)$$

The goodness of fit between the experimental data and the proposed isotherm models was determined using regression analysis results shown in Fig. 11a-c. The most suitable isotherm model was selected according to the degree of correlation between experimental and theoretical data as indicated by the R^2 value (Table-6). By comparing the R^2 values of all tested models, it was clear that all developed materials exhibited MeB adsorption best fitted to the Langmuir model with a correlation coefficient R^2 ranging from 0.968 to 0.989. Therefore, the adsorption mechanism is monolayer chemisorption. The order of the calculated monolayer maximum capacity (q_{max}) from the Langmuir model is MCF105 > MCF103 > MCF101, which follows the kinetic adsorption findings.

The high value of q_{max} (> 28 mg g^{-1}) indicated a strong interaction between MeB and the $Mg_xCo_{1-x}Fe_2O_4$/polyol materials and the removal process proceeded *via* monolayer chemical adsorption. The separation factor (R_L) of all materials had values ranging from 0.107 to 0.964 (between $0 > R_L < 1$) approved the favourable adsorption of MeB onto the Mg_xCo_{1-x} Fe_2O_4/polyol. In addition, the Freundlich constant (K_F), ranged from 16-251 L $g^{-1,}$ which is related to the adsorption capacity and is higher than both the experimental and Langmuir values demonstrated good adsorption affinity towards MeB. Moreover, the values of the n constants were 1.064 and 1.122 (n > 1) for MCF103 and MCF105, respectively, indicating a favourable adsorption process. On the other hand, material MCF101 exhibited an n value below 0.801, which is consistent with weaker adsorption than MCF103 and MCF105, whereas a (1/n) value higher than unity is characteristic of cooperative adsorption.

For MCF103 and MCF105, the (1/n) values were below 0.939, which is characteristic of adsorption on heterogeneous

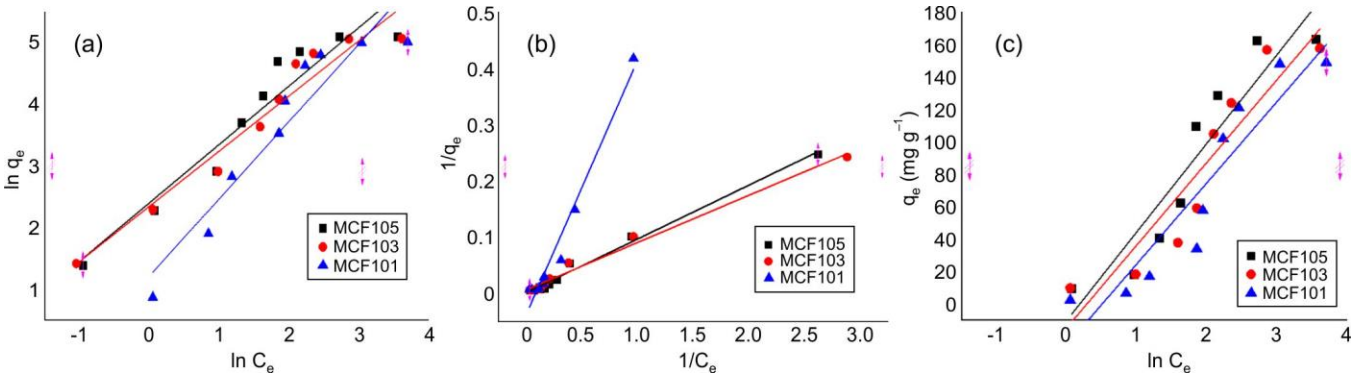

Fig. 11. (a) Langmuir, (b) Freundlich and (c) Temkin isotherm model for MeB adsorption to $Mg_xCo_{1-x}Fe_2O_4$/polyol materials

TABLE-6
ADSORPTION ISOTHERM PARAMETERS FOR MeB DYE ADSORPTION ONTO $Mg_xCo_{1-x}Fe_2O_4$/POLYOL MATERIAL

Isotherm model	Parameter	MCF101	MCF103	MCF105
Experimental	q_{max} (mg g^{-1})	148.0	157.4	163.2
Langmuir model	q_{max} (mg g^{-1})	28.1	143.7	568.2
	K_L (L mg^{-1})	0.0789	0.0832	0.0184
	R_L	0.1124-0.863	0.107-0.857	0.352-0.964
	R^2	0.968	0.984	0.989
Freundlich model	n	0.801	1.122	1.064
	K_F	16.6	218.7	251.2
	R^2	0.879	0.937	0.905
Temkin model	B (J mol^{-1})	49.8	50.8	54.4
	A_T (L g^{-1})	0.318	0.529	0.665
	b_T (J mol^{-1})	49.8	48.8	45.5
	R^2	0.852	0.845	0.855

surfaces. The Freundlich constants confirm the strong affinity of MeB towards the developed adsorbents. The adsorption process is likely initiated by the transport of MeB molecules from the bulk solution to the adsorbent surface, followed by their accumulation at the available active sites.

The Temkin isotherm was evaluated using the experimental data and the corresponding plots are shown in Fig. 11c. Correlation coefficients in the range of 0.845-0.855 were obtained, which were lower than those associated with the Langmuir model, confirming the limited applicability of the Temkin isotherm to the present adsorption system. The Temkin binding constant (A_T) varied from 0.318 to 0.665 L g^{-1} exhibit favourable interactions between MeB molecules and the adsorbent surface. The adsorption heat constant (b_T) ranged from 45.5 to 49.8 J mol^{-1}, whereas the B constant remained positive within the range of 49.8-54.4 J mol^{-1}, consistent with an endothermic adsorption process. The combined isotherm and kinetic analyses support adsorption through surface diffusion and pseudo-second-order kinetics with monolayer adsorption dominating the process.

Recyclability of adsorbents: The recyclability of the developed materials was examined by testing the profile of the adsorption removal, ten cycles of adsorption-desorption utilizing the same material. The successive experiments were conducted under optimal adsorption from 50 mL of MeB sample at a concentration of 5 mg L^{-1} mixed with 0.05 g of adsorbent and a stirring time of 60 min. MCF103 sample was selected as the representative adsorbent for regeneration studies due to its intermediate Mg content among the investigated materials. Previous elution experiments identified HCl as the most effective desorbing agent compared with HNO_3 and methanol. HCl concentrations above 0.2 M achieved MeB recoveries exceeding 95% for MCF101, MCF103 and MCF105 (Fig. 12a). A 0.25 M HCl solution was therefore selected for subsequent desorption experiments.

The recyclability results presented in Fig. 12b show that the MeB recovery remained above 90% with a loss of less than 5% after six adsorption-desorption cycles. These results confirmed that the developed MCF-based adsorbents retain high adsorption efficiency over repeated use. A gradual decrease in recovery beyond six cycles can be attributed to the loss or deactivation of active adsorption sites on the adsorbent surface.

Comparison to other MeB adsorbents: The developed $Mg_xCo_{1-x}Fe_2O_4$/polyol-based materials had an extremely high adsorption capacity for MeB compared with many reported adsorbents, as shown in Table-7. These include silver titanate [39], bismuth ferrite [41] and cobalt zinc ferrite [42]. Other materials showed approximately one-third of the current adsorbents, such as Fe-doped N-rich fiberboard char [40] and magnesium ferrite [43]. Other adsorbents showed a capacity comparable to that of coal fly ash [44] or much higher, such as chitosan-phthalic anhydride/ZrO_2 [38], than the proposed materials. The easy preparation, low cost and eco-friendly nature of these materials have given them an advantage over other costly adsorbents. In addition, the adsorption capacity of all the developed phases was sufficient for the removal of MeB molecules from real-world water samples, making them

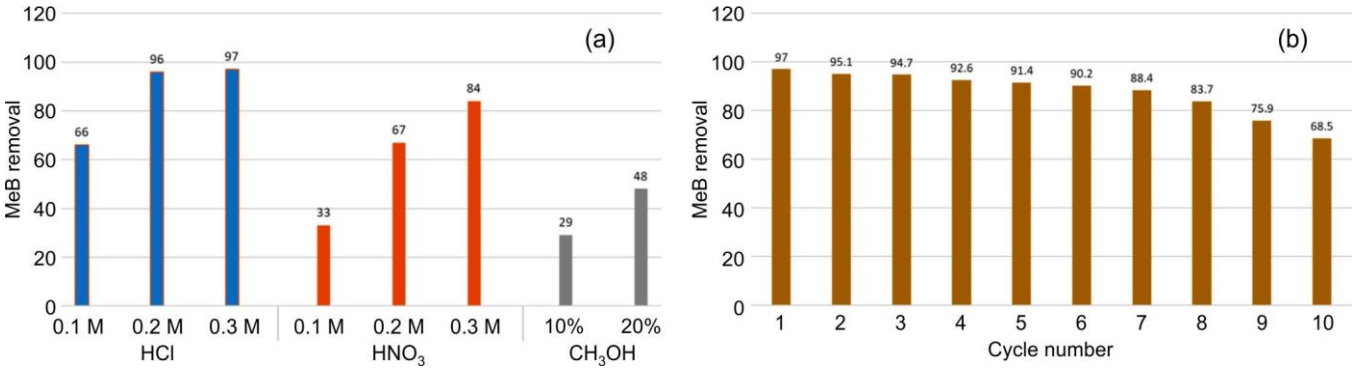

Fig. 12. Testing various eluents for MeB desorption from MCF103 NPs/polyol nanocomposite (a) and recyclability of MCF103/polyol for adsorptive removal of MeB dye (b)

TABLE-7
COMPARISON OF THE ADSORPTION CAPACITY OF THE DEVELOPED $Mg_xCo_{1-x}Fe_2O_4$/POLYOL-BASED MATERIALS WITH VARIOUS REPORTED MATERIALS FOR MeB DYE REMOVAL

Adsorbent	pH	Maximum capacity (mg g^{-1})	Ref.
$Mg_{0.1}Co_{0.9}Fe_2O_4$/polyol	6.5	148.0	This work
$Mg_{0.3}Co_{0.7}Fe_2O_4$/polyol		157.4	
$Mg_{0.5}Co_{0.5}Fe_2O_4$/polyol		163.2	
Silver titanate	3	5.24	[38]
Bismuth ferrite	–	7.14	[39]
Cobalt-zinc ferrite	Natural pH	3.4	[40]
Fe-doped N-rich fiberboard char	–	56.6	[41]
Magnesium ferrite	–	57.7	[42]
Coal fly ash	8	151.0	[43]
Chitosan-phthalic anhydride/ZrO_2	9.8	240.1	[44]

alternative water treatment techniques that can have many applications in industry and water treatment.

Conclusion

In conclusion, magnesium-doped cobalt nanoferrites (x = 0.1, 0.3, 0.5) $Mg_xCo_{1-x}Fe_2O_4$NPs were successfully synthesised *via* a polyol route. XRD results verified the successful formation of a single-phase cubic spinel structure, whereas SEM and TEM reconfirmed a uniform spherical morphology with nanoscale dimensions (~12 nm). The adsorption process followed pseudo-second-order kinetics, with the synthesised material exhibiting high adsorption efficiency toward the target pollutant. The addition of Mg to the spinel ferrite structure drastically altered its crystalline characteristics, optical response and adsorption activity. The $Mg_{0.5}Co_{0.5}Fe_2O_4$ nanoferrites showed impressive efficiency, making it suitable for environmental purification applications, particularly in the degradation of organic waste. These results confirm the successful formation of nanoscale $Mg_xCo_{1-x}Fe_2O_4$ particles with controlled sizes and morphologies which are suitable for the advanced functional applications.

ACKNOWLEDGEMENTS

The authors acknowledge with thanks DSR for technical and financial support. They also extend their gratitude to the Chhatrapati Shahu Maharaj Research, Training and Human Development Institute (SARTHI), Government of Maharashtra, for its financial assistance. The authors also thank to Deanship of Scientific Research at Shaqra University for supporting this work.

CONFLICT OF INTEREST

The authors declare that there is no conflict of interests regarding the publication of this article.

DECLARATION OF AI-ASSISTED TECHNOLOGIES

During the preparation of this manuscript, the authors used an AI-assisted tool(s) to improve the language and no data, results or scientific conclusions were generated by AI. All analyses, interpretations and conclusions are the authors' own. The authors reviewed and edited the content and take full responsibility for the published work.

REFERENCES

1. S. Shindhal, P. Rakholiya, S. Varjani, A. Pandey, H.H. Ngo, W. Guo, H.Y. Ng and M.J. Taherzadeh, *Bioengineered*, **12**, 70 (2021); https://doi.org/10.1080/21655979.2020.1863034
2. F. Un Nisa, K. Naseem, A. Aziz, W. Hassan, N. Fatima, J. Najeeb, S. U. Rehman, A. Khalid and M.E. Khan, *Rev. Inorg. Chem.*, **45**, 275 (2025); https://doi.org/10.1515/revic-2024-0042
3. A. Mishra, S. Takkar, N.C. Joshi, S. Shukla, K. Shukla, A. Singh, A. Manikonda and A. Varma, *Front. Microbiol.*, **12**, 802544 (2022); https://doi.org/10.3389/fmicb.2021.802544
4. P. Kumar, K. Singh, J. Singh, M. K. Talla, S. Ali, R. Chauhan, and A. Ranjan, *J. Environ. Eng.*, **152**, 03126008 (2026); https://doi.org/10.1061/JOEEDU.EEENG-8462
5. A. Rane and S. J. Joshi, *Open Biotechnol. J.*, **15**, 97 (2021); https://doi.org/10.2174/1874070702115010097
6. M. Kumar, V.P. Singh, S.B. Bhat and R. Kumar, *Discov. Environ.*, **3**, 132 (2025); https://doi.org/10.1007/s44274-025-00337-0
7. M. Tripathi, S. Singh, S. Pathak, J. Kasaudhan, A. Mishra, S. Bala, D. Garg, R. Singh, P. Singh, P.K. Singh, A.K. Shukla and N. Pathak, *Toxics*, **11**, 940 (2023); https://doi.org/10.3390/toxics11110940
8. F. Mohamadpour and A.M. Amani, *RSC Adv.*, **14**, 20609 (2024); https://doi.org/10.1039/D4RA03259D
9. R. Shah, D. Khan, A. Al-Anazi, W. Ahmad, I. Ullah, N.S. Shah and J.A. Khan, *Appl. Catal. O: Open*, **204**, 207043 (2025); https://doi.org/10.1016/j.apcato.2025.207043

10. S. Das, L. Cherwoo and R. Singh, *Biotechnol. Notes*, **4**, 64 (2023); https://doi.org/10.1016/j.biotno.2023.10.001
11. A.A. Najim, A.Y. Radeef and Z.H. Jabbar, *Chem. Eng. Res. Design*, **219**, 198 (2025); https://doi.org/10.1016/j.cherd.2025.06.005
12. S. Satyam and S. Patra, Heliyon, **10**, e29573 (2024); https://doi.org/10.1016/j.heliyon.2024.e29573
13. T. Alsawy, E. Rashad, M. El-Qelish and R.H. Mohammed, *npj Clean Water*, **5**, 29 (2022); https://doi.org/10.1038/s41545-022-00172-3
14. S. Mileta and I. Nuić, *Sustainability*, **18**, 6673 (2026); https://doi.org/10.3390/su18136673
15. S. Meftah, K. Meftah, M. Addich and A. Chahid, *Discov. Environ.*, **4**, 257 (2026); https://doi.org/10.1007/s44274-026-00769-2
16. G. Crini and E. Lichtfouse, *Environ. Chem. Lett.*, **17**, 145 (2019); https://doi.org/10.1007/s10311-018-0785-9
17. A. Soltani, M. Faramarzi and S.A. Mousavi Parsa, *Water Qual. Res. J.*, **56**, 181 (2021); https://doi.org/10.2166/wqrj.2021.023
18. M.T. Yagub, T.K. Sen, S. Afroze and H.M. Ang, *Adv. Colloid Interface Sci.*, **209**, 172 (2014); https://doi.org/10.1016/j.cis.2014.04.002
19. W. Hou and Z. Wang, *J. Sol-Gel Sci. Technol.*, **79**, 543 (2016); https://doi.org/10.1007/s10971-016-4168-z
20. M.B. Mohamed and M. Yehia, *J. Alloys Compd.*, **615**, 181 (2014); https://doi.org/10.1016/j.jallcom.2014.06.156
21. M. Basak, M.L. Rahman, M.F. Ahmed, B. Biswas and N. Sharmin, *J. Alloys Compd.*, **895**, 162694 (2022); https://doi.org/10.1016/j.jallcom.2021.162694
22. S.H. Khoreem and A.H. AL-Hammadi, *Discov. Mater.*, **5**, 173 (2025); https://doi.org/10.1007/s43939-025-00374-9
23. S.H. Khoreem and A.H. AL-Hammadi, *Discov. Nano*, **20**, 3 (2025); https://doi.org/10.1186/s11671-024-04180-9
24. S. Kalingani, S. Das and S. Bhuyan, *Inorg. Chem. Commun.*, **159**, 111731 (2024); https://doi.org/10.1016/j.inoche.2023.111731
25. S.H. Khoreem and A.H. Al-Hammadi, *Biointerface Res. Appl. Chem.*, **13**, 488 (2023); https://doi.org/10.33263/BRIAC135.488
26. R. Kumar, R. Jasrotia, Himanshi, J. Ahmed, A. Vidya Nidhi, S.M. Alshehri, L.W.Y. Liu, S.A. Patil, R. Aggarwal, S. Kumar Godara, P.B. Barman, R.R. Singh and A. Kandwal, *Inorg. Chem. Commun.*, **157**, 111355 (2023); https://doi.org/10.1016/j.inoche.2023.111355
27. O. Oulhakem, I. Guetni, M. Elansary, Y. Mouhib, M. Belaiche and K. Belrhiti Alaoui, *Appl. Phys., A Mater. Sci. Process.*, **127**, 814 (2021); https://doi.org/10.1007/s00339-021-04941-8
28. S.M. Suryawanshi, D.S. Badwaik, B.S. Shinde, K.D. Gaikwad, M. Shkir, K.V. Chandekar and S. Gundale, *J. Mol. Struct.*, **1272**, 134173 (2023); https://doi.org/10.1016/j.molstruc.2022.134173
29. C. Aziz and B. Azhdar, *J. Magn. Magn. Mater.*, **542**, 168577 (2022); https://doi.org/10.1016/j.jmmm.2021.168577
30. M. Kosmulski, *Adv. Colloid Interface Sci.*, **319**, 102973 (2023); https://doi.org/10.1016/j.cis.2023.102973
31. M.R. Patil and V.S. Shrivastava, *Desalination Water Treat.*, **57**, 5879 (2016); https://doi.org/10.1080/19443994.2015.1004594
32. Y.S. Ho and G. McKay, *Chem. Eng. J.*, **70**, 115 (1998); https://doi.org/10.1016/S0923-0467(98)00076-1
33. Y.S. Ho, G. McKay, D.A.J. Wase and C.F. Forster, *Adsorpt. Sci. Technol.*, **18**, 639 (2000); https://doi.org/10.1260/0263617001493693
34. W.J. Weber Jr. and J.C. Morris, *J. Sanitat. Eng. Division ASCE*, **89**, 31 (1963); https://doi.org/10.1061/JSEDAI.0000430
35. I. Langmuir, *J. Am. Chem. Soc.*, **40**, 1361 (1918); https://doi.org/10.1021/ja02242a004
36. Y.S. Ho and G. McKay, *J. Phys. Chem.*, **57**, 385 (1998); https://doi.org/10.1016/S0923-0467(98)00076-1
37. M. Kondalkar, U. Fegade, S. Inamuddin, S. Kanchi, T. Altalhi, K.E. Suryawanshi and A.M. Patil, *J. Phys. Chem. Solids*, **163**, 110544 (2022); https://doi.org/10.1016/j.jpcs.2021.110544
38. N.R. Shefa, M.A. Khatun, A.H. Jalal, M.J. Uddin and M.W. Rahman, *Clean. Chem. Eng.*, **11**, 100163 (2025); https://doi.org/10.1016/j.clce.2025.100163
39. S. Singh, Y. Yadawa and A. Ranjan, *J. Environ. Chem. Eng.*, **11**, 109229 (2023); https://doi.org/10.1016/j.jece.2022.109229
40. T. Tatarchuk, N. Paliychuk, R.B. Bitra, A. Shyichuk, M. Naushad, I. Mironyuk and D. Ziółkowska, *Desalination Water Treat.*, **150**, 374 (2019); https://doi.org/10.5004/dwt.2019.23751
41. M. Zhao, D. Ji, G. Wu and Y. Wu, *Ind. Crops Prod.*, **220**, 119249 (2024); https://doi.org/10.1016/j.indcrop.2024.119249
42. A. Ivanets, V. Prozorovich, M. Roshchina, O. Sychova, V. Srivastava and M. Sillanpää, *Mater. Today Commun.*, **31**, 103594 (2022); https://doi.org/10.1016/j.mtcomm.2022.103594
43. M. Kurniasih, N.H. Aprilita, R. Roto and M. Mudasir, *Case Stud. Chem. Environ. Eng.*, **11**, 101101 (2025); https://doi.org/10.1016/j.cscee.2025.101101
44. A.S. Abdulhameed, R.H. Al Omari, M.K. Younes and S. Algburi, *J. Mol. Struct.*, **1339**, 142386 (2025); https://doi.org/10.1016/j.molstruc.2025.142386